CORA Cork Open Research Archive
Cartlann Taighde Oscailte Chorcaí

Title	Engineering the interface chemistry for scandium electron contacts in WSe2 transistors and diodes
Authors	Smyth, Christopher M.;Walsh, Lee A.;Bolshakov, Pavel;Catalano, Massimo;Schmidt, Michael;Sheehan, Brendan;Addou, Rafik;Wang, Luhua;Kim, Jiyoung;Kim, Moon J.;Young, Chadwin D.;Hinkle, Christopher L.;Wallace, Robert M.
Publication date	2019-07-24
Original Citation	Smyth, C. M., Walsh, L. A., Bolshakov, P., Catalano, M., Schmidt, M., Sheehan, B., Addou, R., Wang, L., Kim, J., Kim, M. J., Young, C. D., Hinkle, C. L. and Wallace, R. M. (2019) 'Engineering the interface chemistry for scandium electron contacts in WSe2 transistors and diodes', 2D Materials, 6(4), 045020. (17pp.) DOI: 10.1088/2053-1583/ab2c44
Type of publication	Article (peer-reviewed)
Link to publisher's version	https://iopscience.iop.org/article/10.1088/2053-1583/ab2c44 - 10.1088/2053-1583/ab2c44
Rights	©Original content from this work may be used under the terms of the Creative Commons Attribution 3.0 licence. Any further distribution of this work must maintain attribution to the author(s) and the title of the work, journal citation and DOI. - https://creativecommons.org/licenses/by/3.0/
Download date	2026-10-31 13:58:34
Item downloaded from	https://hdl.handle.net/10468/8476



UCC
University College Cork, Ireland
Coláiste na hOllscoile Corcaigh

2D Materials

PAPER • **OPEN ACCESS**

Engineering the interface chemistry for scandium electron contacts in WSe_2 transistors and diodes

To cite this article: Christopher M Smyth *et al* 2019 *2D Mater.* **6** 045020

View the article online for updates and enhancements.

This content was downloaded from IP address 143.239.102.117 on 09/09/2019 at 11:59

2D Materials

OPEN ACCESS

RECEIVED
26 March 2019

REVISED
29 May 2019

ACCEPTED FOR PUBLICATION
24 June 2019

PUBLISHED
24 July 2019

Original content from this work may be used under the terms of the Creative Commons Attribution 3.0 licence.

Any further distribution of this work must maintain attribution to the author(s) and the title of the work, journal citation and DOI.

PAPER

Engineering the interface chemistry for scandium electron contacts in WSe_2 transistors and diodes

Christopher M Smyth[1], Lee A Walsh[1,2], Pavel Bolshakov[1], Massimo Catalano[1,3], Michael Schmidt[2], Brendan Sheehan[2], Rafik Addou[4], Luhua Wang[1], Jiyoung Kim[1], Moon J Kim[1], Chadwin D Young[1], Christopher L Hinkle[1,5] and Robert M Wallace[1]

[1] Department of Materials Science and Engineering, University of Texas at Dallas, Richardson, TX 75080, United States of America
[2] Tyndall National Institute, Lee Maltings Complex, Dyke Parade, Cork T12R5CP, Ireland
[3] CNR IMM, Institute for Microelectronics and Microsystems, Via Monteroni, I-73100 Lecce, Italy
[4] School of Chemical, Biological and Environmental Engineering, Oregon State University, Corvallis, OR 97331, United States of America
[5] Department of Electrical Engineering, University of Notre Dame, Notre Dame, IN 46556, United States of America

E-mail: rmwallace@utdallas.edu

Keywords: metal contact, transistor, WSe_2, scandium, interfacial chemistry, anneal, x-ray photoelectron spectroscopy

Supplementary material for this article is available online

Abstract

Sc has been employed as an electron contact to a number of two-dimensional (2D) materials (e.g. MoS_2, black phosphorous) and has enabled, at times, the lowest electron contact resistance. However, the extremely reactive nature of Sc leads to stringent processing requirements and metastable device performance with no true understanding of how to achieve consistent, high-performance Sc contacts. In this work, WSe_2 transistors with impressive subthreshold slope (109 mV dec^{-1}) and I_{ON}/I_{OFF} (10^6) are demonstrated without post-metallization processing by depositing Sc contacts in ultra-high vacuum (UHV) at room temperature (RT). The lowest electron Schottky barrier height (SBH) is achieved by mildly oxidizing the WSe_2 *in situ* before metallization, which minimizes subsequent reactions between Sc and WSe_2. Post metallization anneals in reducing environments (UHV, forming gas) degrade the I_{ON}/I_{OFF} by ~10^3 and increase the subthreshold slope by a factor of 10. X-ray photoelectron spectroscopy indicates the anneals increase the electron SBH by 0.4–0.5 eV and correspondingly convert 100% of the deposited Sc contacts to intermetallic or scandium oxide. Raman spectroscopy and scanning transmission electron microscopy highlight the highly exothermic reactions between Sc and WSe_2, which consume at least one layer RT and at least three layers after the 400 °C anneals. The observed layer consumption necessitates multiple sacrificial WSe_2 layers during fabrication. Scanning tunneling microscopy/spectroscopy elucidate the enhanced local density of states below the WSe_2 Fermi level around individual Sc atoms in the WSe_2 lattice, which directly connects the scandium selenide intermetallic with the unexpectedly large electron SBH. The interface chemistry and structural properties are correlated with Sc–WSe_2 transistor and diode performance. The recommended combination of processing conditions and steps is provided to facilitate consistent Sc contacts to WSe_2.

Introduction

Continuous engineering of contacts compatible with state-of-the-art semiconductor technology relies upon a detailed understanding of the critical relationships between processing conditions, interface chemistry and structure, and contact performance [1]. Silicides [2] and salicides [3, 4] exhibit a broad spectrum of composition-dependent contact resistances (R_c) and have long been employed as standard, low resistance contacts in traditional (Si, Ge) and compound (e.g. InGaAs) semiconductor-based CMOS technologies. Similar interface engineering has only recently been explored to improve Pd contacts to WSe_2 [5], a semiconducting member of the transition metal dichalcogenide (TMD) family of two-dimensional (2D) materials, and is a promising, versatile strategy to engineer high-performance contacts comparable with Si technology ($R_c \approx 50\ \Omega$ cm) [6].

© 2019 IOP Publishing Ltd

High defect concentrations ($>10^{18}$ cm^{-3}) [7–9], metal-TMD and metal-ambient gas reaction products [10–12], and spurious electrostatic effects [13, 14] often manifest as strong E_F pinning [15] and/or large parasitic R_c, which can convolute the intrinsic properties (e.g. mobility) of a TMD-based device [16, 17]. A number of strategies have been employed to reduce R_c to TMDs, with varying degrees of success [18–24]. However, many are incompatible with typical back-end-of-line (BEOL) process flows, and direct metallization in top contacted devices is preferred. Impressive electron contact performance in MoS_2 and black phosphorous (BP) devices has been demonstrated with Sc contacts [25–27]. However, Sc has yet to be explored as a contact metal in WSe_2-based devices. Furthermore, the highly reactive nature of Sc lends to processing difficulties and metastable device performance [26, 27]. Sc spontaneously forms scandium oxide, a high-κ dielectric with a 5–6 eV band gap [28], even in ultra-high vacuum (UHV) conditions [10] and when a capping layer is employed to limit spurious air-exposure induced effects. Therefore, engineering high-performance Sc contacts to WSe_2 requires a detailed understanding of the relationship between processing conditions, interface chemistry, and Sc contact performance.

WSe_2 is also a promising alternative 2D switch in state-of-the-art magnetoresistive random-access memory technology due to the giant spin splitting in the valence band (456 meV) [29], moderate hole mobility [15], and low switching power. Spin-torque transfer based on the spin-valley Hall effect in WSe_2 has emerged as a preferred magnetic bit-writing method in analogous devices [30] but relies on a single WSe_2 layer, which can experience catastrophic damage during processing. Before the technology can be integrated in commercial applications, the effects of common BEOL processing conditions on the integrity of the WSe_2 monolayer must be quantified.

In this work, we establish relationships between processing conditions (deposition chamber ambient, post-metallization annealing temperature and ambient), interface chemistry, and band alignment in the Sc–WSe_2 system with *in situ* x-ray photoelectron spectroscopy (XPS) experiments. The number of WSe_2 layers consumed by reactions with Sc after fabrication, 300 °C post-metallization anneals, and as a function of time between fabrication and characterization are quantified with Raman spectroscopy, scanning transmission electron microscopy (STEM), and energy dispersive x-ray spectroscopy (EDS). Scanning tunneling microscopy/spectroscopy (STM/STS) elucidate the effects of Sc atoms on the local density of WSe_2 surface states, providing insight into the extracted band alignment. We demonstrate moderate E_F depinning in metal-WSe_2 systems by deliberate growth of a scandium oxide depinning layer at the contact-WSe_2 interface. Finally, we evaluate the electrical performance of UHV-deposited Sc contacts to WSe_2 field-effect transistors (FETs) as a function of post-metallization annealing conditions. Recommendations are provided to preserve the high-performance Sc electron contacts to WSe_2 and to alleviate E_F pinning in metal-WSe_2 systems, which are based upon the impressive FET performance metrics and band alignment control demonstrated here.

Methods

Metallization, annealing, and *in situ* characterization

(a) Depositing 1 nm Sc in UHV or high vacuum (HV): The synthetic WSe_2 crystals employed in this work were purchased from HQ Graphene [31]. Before performing electron beam evaporation of Sc in UHV or HV, materials (WSe_2, Sc metal) were prepared, the metal deposition rate was determined, and reference core level spectra were obtained identical to that employed and described in our previous work [10, 11]. Metal deposition was performed in UHV and HV using a similar base pressure of $< 2 \times 10^{-9}$ and deposition pressures of 7×10^{-9} mbar and 5×10^{-6} mbar, respectively. The Sc depositions in HV and UHV were performed in the same chamber. However, the deposition in HV was performed by first ramping the filament current up to the deposition current under UHV conditions, then backfilling the chamber with air to a pressure of 5×10^{-6} mbar, and subsequently opening the shutters to start the deposition. This method permits *in situ* XPS characterization after Sc deposition in HV unlike when the deposition is performed *ex situ*. A 50 nm thick Sc film was deposited on highly oriented pyrolytic graphite (HOPG) at RT in UHV and the reference Sc 2*p* core level spectrum was immediately obtained *in situ*.

(b) Step-wise Deposition and Post-Metallization Annealing: All Sc depositions, anneals, and XPS characterization were performed in a cluster tool described elsewhere [32, 33]. Sc was deposited in UHV on separate bulk WSe_2 crystals to estimated thicknesses of 0.1, 0.2, 1.0, 2.0, and 5.0 nm. Consecutive annealing steps were subsequently performed on each sample in UHV or forming gas (FG; 5% H_2, 95% N_2; 1 mbar) at 200 °C, 300 °C, and 400 °C for 1 h each. The stainless steel gas line connecting the FG cylinder to the annealing chamber was pumped overnight to a pressure of $<2 \times 10^{-9}$ mbar to remove any adsorbed species (i.e. H_2O) from within the gas line before the chamber was backfilled

with FG and the anneal was performed. XPS was performed after exfoliation and each subsequent deposition and annealing step to characterize the surface chemistry and the secondary electron cutoff. The secondary electron cutoff was measured to track the work function. The procedures employed to fit high-resolution core level spectra and construct band diagrams are discussed in detail in the supporting information (stacks.iop.org/TDM/6/045020/mmedia).

XPS instrumentation, parameters, and data analysis

XPS characterization was performed via a A monochromated Al Kα source and hemispherical analyzer (Omicron EA125) with ±0.05 eV resolution were employed for XPS. The cross sectional area of the incident x-ray beam is ~7.85×10^{-3} cm^2. A 45° takeoff angle, 8° acceptance angle, and 15 eV pass energy were employed when acquiring high-resolution spectra. The analyzer was calibrated according to ASTM E1208 [34]. Spectra were deconvolved using the curve fitting software AAnalyzer [35].

Quantifying layer number consumption: sample fabrication and characterization

WSe_2 flakes onto a SiO_2/Si substrate (270 nm thermal SiO_2). After transferring the samples into the cluster tool, the annealing chamber was pumped to a base pressure of $< 2 \times 10^{-8}$ mbar and then backfilled with Ar to 1 bar before annealing at 300 °C for 1 h to remove organic tape residue. Many 1 to 5 layer (1L to 5L) flakes were identified with optical microscopy, atomic force microscopy (AFM), and Raman spectroscopy. 5 nm thick Sc films were then deposited in UHV onto the WSe_2 flakes (see supporting information for more details). Immediately after metallization, select samples were annealed *in situ* in UHV or FG at 300 °C for 1 h. A full coverage, 10 nm thick Si capping layer was subsequently deposited *in situ* using electron beam evaporation to protect the Sc–WSe_2 heterostructure from spurious air-induced reactions during *ex situ* Raman spectroscopy. The anneals were performed before depositing the Si cap to prevent intermixing between Si and the underlying Sc–WSe_2 heterostructure at elevated temperatures.

All Raman spectra were obtained using a laser power density of 0.49 mW μm^{-2} and a 0.2 cm^{-1} detector resolution. The Raman spectra were obtained from exfoliated WSe_2 flakes after the vacuum anneal with 1 s exposure time and ten accumulations. After metallization and annealing (where applicable), Raman spectra were obtained using a 5 s exposure time and five accumulations. These parameters were carefully tuned to prevent laser-induced damage to WSe_2 (see [5] for details regarding our carefully optimized Raman spectroscopy parameters).

Raman spectra were deconvolved with AAnalyzer to rigorously determine Raman shifts. A combination of Gaussian and Lorentzian functions was employed in the fitting process. The Lorentzian contribution varied with the number of WSe_2 layers in the probed region and was therefore held constant for each set of spectra representing a certain number of WSe_2 layers.

STEM and EDS

(a) Lamella were milled from the Si/Sc/WSe_2/SiO_2 samples, which were initially fabricated for characterization by Raman spectroscopy, using a FIB electron microscope (FEI Nova 200 Dual Beam). High-resolution STEM was performed in an aberration corrected JEM-ARM200F instrument operated at 200 kV. Images were obtained using annular bright field and high angle annular dark field modes. EDS experiments were performed in an Aztec Energy Advanced Microanalysis System according to the procedure outlined in detail elsewhere [33]. EDS line scan data were acquired point by point (acquisition time ~0.5 s/pixel), which minimizes radiation damage in the lamella and increases the noise level in the data.

(b) A lamella from a 65 nm Pd/5 nm Sc/WSe_2 diode treated with atomic hydrogen (see below for details) was cross sectioned using an FEI Dual Beam Helios Nanolab 600i SEM/FIB microscope. Annular bright field TEM images were obtained with a JEOL 2100 operated at 200 kV.

Device fabrication

(a) The backside gate dielectric was formed by depositing a 27 nm Al_2O_3 film onto a Si wafer (p++) at 250 °C and subsequently annealing the wafer at 400 °C in FG to reduce charge traps [36]. Al was then deposited by electron beam evaporation on the reverse side of the Si wafer as the backside contact. After exfoliating WSe_2 flakes onto the Al_2O_3, source/drain contacts were defined using photolithography and Sc/Pd (20 nm/50 nm) contacts were subsequently deposited in UHV by electron beam evaporation. The sample was then transferred *ex situ* to an elastomer sealed electron beam deposition tool where 100 nm Au was deposited on top of the Sc/Pd layers. Finally, a lift-off process was performed. The devices were electrically characterized in air at RT and 1 bar in a Cascade Probe Station using a Keithley 4200 Semiconductor Characterization System.

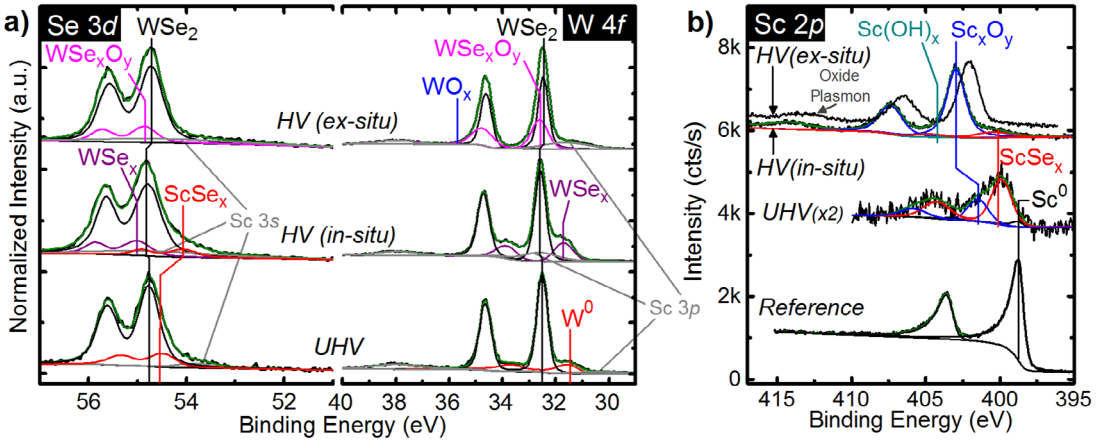


Figure 1. (a) Se 3*d*, W 4*f*, and (b) Sc 2*p* core level spectra obtained *in situ* after Sc deposition in UHV and HV on bulk WSe_2 (base pressure $<2 \times 10^{-9}$ mbar in each case, see Methods for details on the deposition in HV). Significant reactions occur between Sc, WSe_2, and background gases in the chamber, which completely convert Sc and $ScSe_x$ to Sc_xO_y when the deposition is performed in HV.

(b) Schottky Diodes: A bulk WSe_2 crystal was exfoliated, resulting in a mirror-like (presumably low defect density) surface, and loaded into a UHV cluster tool [32, 33]. Select samples were treated with atomic hydrogen *in situ* prior to metallization.
Sc/Pd contacts (65 nm Pd, see main text for Sc thickness details) were deposited through a shadow mask in UHV and 100 nm Au was subsequently deposited *ex situ* in an elastomer-sealed Temescal BJD-1800 electron beam evaporator [37] (base pressure $< 5 \times 10^{-6}$ mbar) to form arrays of circular contacts (diameters = 50, 100, 200 μm) across the WSe_2 crystal. *I–V* curves were obtained by first sweeping from 0 to 2 V and then from 0 to −2 V (0.01 V step) to prevent hysteresis effects. Measurements were obtained after metallization and subsequent anneals in FG (1 mbar) at 200 °C, 300 °C, and 400 °C. *I–V* curves were obtained from all working diodes, normalized according to the area, and directly compared to confirm the electrical performance scales with area as expected.

Atomic hydrogen treatment
An MBE Komponenten Hydrogen Atom Beam Source (Model No. HCS-40-K-2000654) with tungsten filament was operated at a filament temperature of 1500 °C and a H_2 (99.9999% purity) partial pressure of 5×10^{-6} mbar. The bulk WSe_2 samples were maintained at a substrate temperature of 300 °C throughout the treatment, which was performed for 45 min. After the treatment and cooling to RT, the surface chemistry was characterized with XPS. Contacts were then deposited *in situ*.

Scanning tunneling microscopy and spectroscopy
A bulk WSe_2 crystal was exfoliated and loaded into a UHV cluster tool described elsewhere [33]. The STM/STS images and spectra were acquired at RT in the constant current mode using an etched tungsten tip. Imaging under positive (negative) bias probes filled (empty) surface states within a few eV of the E_F. The conductance (dI/dV versus V) curves obtained in this work are each differentiated averages of 20 curves obtained sequentially at a single location. STM images are processed in the WSxM software.

Results and discussion

Effects of processing conditions on the Sc–WSe_2 interface chemistry and structure

Highly exothermic reactions between Sc, WSe_2, and background gases in vacuum
The metal–semiconductor interface chemistry can vary significantly with the deposition chamber base pressure and the deposition rate [10–12, 38]. According to the kinetic theory of gases, the impingement rate of background gases on the substrate during deposition in HV is sufficiently high for continuous metal oxidation on the substrate surface. In addition, the reaction products formed between highly reactive metals, such as Sc, and TMDs also undergo exothermic reactions with the background ambient, complicating the interface chemistry further.

Sc aggressively reacts with WSe_2 when deposited at RT regardless of the deposition chamber base pressure. Figure 1(a) shows the Se 3*d* and W 4*f* core level spectra obtained from exfoliated, bulk WSe_2 after depositing ~1 nm Sc at RT in UHV or HV. When deposited in UHV, Sc completely reduces WSe_2 to form metallic W and $ScSe_x$. The presence of metallic W is confirmed by the binding energy (BE) of the asymmetrically shaped, low BE chemical state in the corresponding W 4*f* core level spectrum (W $4f_{7/2}$ BE = 31.30 eV), which is in close agreement with that of a metallic W reference (see Methods for details regarding the metallic W reference). The $ScSe_x$ chemical state in the Se 3*d* core level spectrum is detected at lower BE from the WSe_2 chem-

ical state, which is expected considering, for example, the Pauling scale electronegativity of Sc (1.36) is much less than that of W (2.36) [39].

Our previous work investigating the interface chemistry between transition metals and TMDs have shown that early transition metals typically oxidize *in situ* when deposited in HV [10–12]. However, the HV deposition was performed *ex situ* from the post metallization XPS in [10, 11]. In the aforementioned experimental design, it is difficult to explicitly determine whether the observed oxidation occurs *in situ* during metallization or while transferring the sample between the elastomer-sealed deposition tool and the UHV cluster tool. In this work, the HV Sc deposition was performed in the same chamber as the UHV deposition. However, the chamber was backfilled with air to 5×10^{-6} mbar before the deposition to simulate the conditions typically found in an elastomer sealed deposition tool. This experimental design eliminates any spurious air-exposure induced changes in interface chemistry and elucidates the true chemistry in the Sc–WSe_2 system formed in HV. Sc was also deposited *ex situ* in an elastomer-sealed deposition chamber and subsequently characterized by XPS to compare the Sc–WSe_2 interface chemistry formed in HV with and without air exposure between deposition and XPS.

Sc reduces WSe_2 when deposited in HV with and without the air-exposure step between Sc deposition and XPS. When Sc deposition and subsequent XPS are performed *in situ*, the presence of substoichiometric WSe_x and $ScSe_x$ are evidenced by the chemical states detected at 55.00 eV (31.73 eV) and 54.05 eV, respectively, in the Se 3*d* (W 4*f*) core level spectrum. When the HV Sc deposition and subsequent XPS are performed *ex situ*, the WSe_x that presumably forms as Sc is deposited is oxidized, as evidenced by the appearance of WSe_xO_y and WO_x chemical states at higher BE from the bulk WSe_2 chemical state in the W 4*f* core level (figure 1(a)). However, in a typical contact structure where a thicker Sc film and inert capping metal are employed, WSe_xO_y and WO_x are likely absent from the interface.

The additional grey peaks at low BE relative to the Se 3*d* and W 4*f* core levels correspond with the Sc 3*s* and Sc 3*p* core levels, respectively. The BE and area of these peaks were carefully calibrated according to a Sc reference film to maximize the accuracy of the fit (see supporting information for more details). When deposited in UHV, the majority of the ~1 nm Sc film reacts to form either $ScSe_x$ or Sc_xO_y (figure 1(b)). In contrast, all of the Sc deposited in HV is oxidized (including or excluding air-exposure between deposition and XPS). When Sc is deposited *in situ* in HV, a small concentration of $ScSe_x$ is detected according to the low BE chemical state in the corresponding Sc 2*p* core level spectrum. This indicates that a small concentration of Sc reacts *in situ* with the underlying WSe_2 when deposited in HV. Therefore, a Sc contact deposited in HV is mostly oxidized *in situ*, likely implicating contact performance considering Sc_2O_3 has been employed as a high-κ dielectric [40]. Nearly complete Sc oxidation *in situ* in HV is reasonable considering Sc–O bond formation is highly exothermic ($\Delta G^{\circ}_{f,Sc_2O_3} = -630$ kJ mol^{-1}) compared with the persistence of Sc–Se bonds ($\Delta G^{\circ}_{f,ScSe} = -360$ kJ mol^{-1}) [41]. The presence of Sc_xO_y and $Sc(OH)_x$ are corroborated by the chemical states detected in the corresponding O 1*s* core level (figure S3(b)).

Any reactions between adventitious carbon, which is detected on the exfoliated WSe_2 surface at ~284.4 eV (figure S3(a)), or nitrogen in the background ambient are below the limit of detection. However, when a thicker Sc film is deposited on WSe_2 in UHV, there is evidence for the formation of ScC and/or ScN, which is discussed in greater detail later.

Complete Sc oxidation at elevated temperatures in UHV

A complete understanding of the relationship between processing conditions, interface chemistry, and contact performance is critical to engineering the Sc–WSe_2 interface for high-performance electron transport. Post-metallization annealing can drive additional reactions and concomitant E_F shifts depending on the temperature and ambient. Therefore, the interface chemistry and band alignment between Sc and WSe_2 were tracked *in situ* throughout stepwise Sc deposition in UHV and post metallization annealing (see Methods for experimental details).

Figure 2(a) displays the evolution of integrated intensities of chemical states associated with W^0, $ScSe_x$, Sc_xO_y, and metallic Sc formed after depositing ~5.9 nm Sc on WSe_2 and subsequent UHV anneals. The integrated intensities displayed include both spin orbit split peaks in each of the Sc 2*p*, Se 3*d*, and W 4*f* core levels and are corrected by the appropriate atomic sensitivity factors unique to the detector employed (see supporting information). Sc reacts aggressively with WSe_2 at RT to form metallic W and $ScSe_x$. A complete discussion regarding the evolution of chemical states in the Se 3*d*, W 4*f*, and Sc 2*p* core level spectra throughout Sc deposition at RT up to a total film thickness of 5.9 nm is included in the supporting information. The target Sc film thickness was 5 nm, but deviations from the calibrated deposition rate can manifest as a result of using Sc pellets as the source material instead of a solid Sc slug. In addition, calculating the Sc film thickness from core level attenuation requires the density of the attenuating film, which is difficult to estimate in this particular case considering the complex chemistry, which is discussed below.

The 200 °C UHV anneal drives Sc to react with additional WSe_2, which is evidenced by increases in the intensities of the $ScSe_x$ (50.1% of the total Sc 2*p* core level intensity, figure 2(c)) and metallic W chemical states in the corresponding Se 3*d* and W 4*f* core level spectra (figures 2(a) and S4(a)). However, the concentration of $ScSe_x$ decreases incrementally during

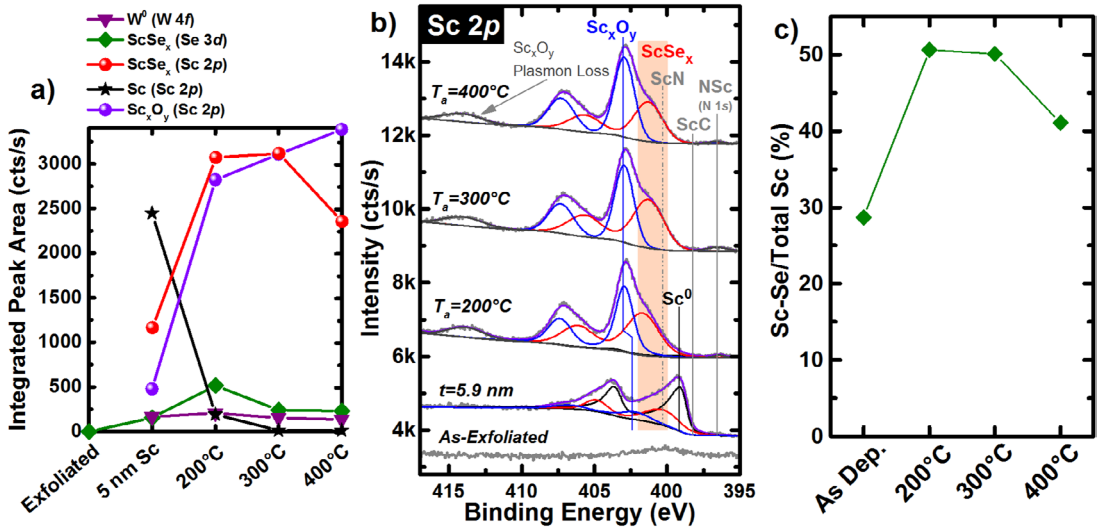


Figure 2. (a) Integrated intensities of chemical states in Se 3*d*, W 4*f*, and Sc 2*p* core level spectra associated with various reaction products as well as the (b) Sc 2*p*, core level spectra obtained from bulk WSe_2 after exfoliation, depositing ~5.9 nm Sc in UHV, and subsequent *in situ* UHV anneals. (c) Percentage of the deposited Sc film converted to $ScSe_x$ after RT deposition and subsequent UHV anneals, which depicts the aggressive reactions between Sc and WSe_2 at RT and moderate intermetallic stability during 200 °C and 300 °C UHV anneals.

the 300 °C and 400 °C UHV anneals, which indicates Sc–Se bonds are dissociated in favor of Sc–O bonds (as predicted by thermodynamics) [41]. In addition, the concentration of metallic W decreases slightly during the 300 °C and 400 °C UHV anneals, which suggests a reaction between metallic W and Se ions liberated from $ScSe_x$ result in the reformation of W–Se bonds (figures 2(a) and S4(a)).

Figure 2(b) shows the Sc 2*p* core level spectrum obtained after depositing 5.9 nm Sc and after each subsequent UHV anneal. 28.7% of the 5.9 nm Sc film is converted to $ScSe_x$ (Sc 2*p*: 400.27 eV) at RT (figures 2(b) and (c)), while the other 71.3% of the film is comprised of a mixture of metallic Sc (398.89 eV), Sc_xO_y (402.16 eV), ScC (397.98 eV), and ScN (400.66 eV). ScC and ScN are near the limit of XPS detection, which is why they are difficult to resolve in figure 2(b). The presence of ScC and ScN in the same Sc–WSe_2 system is validated in the discussion below.

During the 200 °C and 300 °C UHV anneals, all of the deposited metallic Sc either reacts with the underlying WSe_2 to form $ScSe_x$ and metallic W or with the outer ambient to form Sc_xO_y as evidenced by the dramatic intensification of the $ScSe_x$ and Sc_xO_y chemical states in the corresponding Sc 2*p* core level spectrum (figure 2(b)). 17.9% of the $ScSe_x$ formed during the 300 °C UHV anneal is converted to Sc_xO_y during the 400 °C anneal (figure 2), which is thermodynamically favorable [41]. Extending the duration or increasing the temperature of the UHV anneal would presumably increase the relative Sc_xO_y concentration within the film.

After depositing 3.2 nm Sc, a carbidic chemical state is detected at ~281.6 eV in the corresponding C 1*s* core level is detected at 281.60 eV (figure S5), which corroborates the presence of a small concentration of ScC. The formation of Sc–C bonds is exothermic at RT ($\Delta G^{\circ}_{f,ScC} = -164$ kJ mol^{-1}) [42], which suggests ScC is present during initial deposition steps, but below the limit of XPS detection until a total of 3.2 nm Sc is deposited. The BE of the chemical state (~396.5 eV) detected after depositing > 3 nm Sc and throughout subsequent UHV anneals (figure 2(b)) is in good agreement with the ScN chemical state in the N 1*s* core level reported previously [43] and the ScN reference film grown in this work (figure S6). The evolution of chemical states in the C 1*s* core level throughout stepwise Sc deposition and subsequent UHV anneals as well as a detailed chemical analysis of the ScN reference film are discussed further in the supporting information.

Chemical states consistent with Sc_xO_y and $Sc(OH)_x$ species are detected in the O 1*s* core level spectrum throughout the UHV anneals (figure S7) and are discussed in greater detail in the supporting information.

Intermetallic reduction via forming gas annealing

Annealing a TMD device in a partial pressure of H_2 has been shown to passivate defects and improve performance [36, 44, 45]. Therefore, we investigated the effects of FG annealing on the Sc–WSe_2 interface chemistry and band alignment. Prior to performing the FG anneals, stepwise Sc deposition at RT on bulk WSe_2 results in the same Sc film thickness, interface chemistry, and E_F position (figure S8) as were detected prior to the UHV anneals (figure 2).

The 200 °C FG anneal causes the metallic W chemical state in the corresponding W 4*f* core level to shift +0.30 eV and the $ScSe_x$ chemical states in the Se 3*d* and Sc 2*p* core levels to shift −0.35 eV and +1.26 eV, respectively, relative to the chemical states detected after Sc deposition at RT. The aforementioned BE

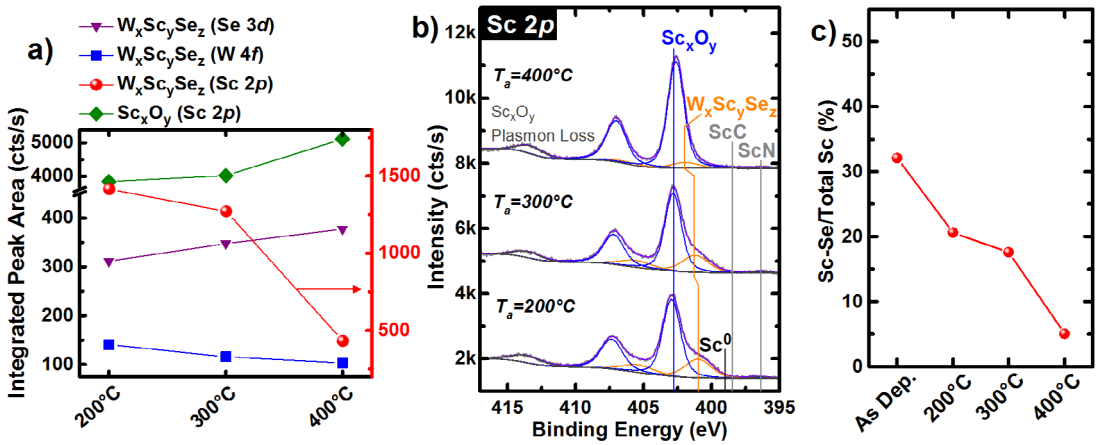


Figure 3. (a) Integrated intensities of the $W_xSc_ySe_z$ intermetallic and Sc_xO_y chemical states in the Se 3*d*, W 4*f*, and Sc 2*p* core level spectra. (b) Sc 2*p* core level spectra obtained from bulk WSe_2 after Sc deposition at RT and subsequent *in situ* FG anneals. (c) Percentage of the deposited Sc film converted to ScSe intermetallic after deposition at RT and subsequent FG anneals showing aggressive reactions at RT and increasing Sc–Se dissociation with increasing FG anneal temperature.

shifts indicate the formation of a ternary $W_xSc_ySe_z$ compound (figures 3(b) and S8). The anneal also dissociates Sc–Se bonds, as evidenced by the small concentration of elemental Se detected at 55.30 eV in the corresponding Se 3*d* core level. Sc–Se bond scission is more favorable than W–Se bond scission considering the relevant bond dissociation energies ($BDE_{Sc–Se} = 385$ kJ mol^{-1}, $BDE_{W–Se} = 418$ kJ mol^{-1}) [46, 47]. After the 400 °C FG anneal, the $W_xSc_ySe_z$ chemical states in the W 4*f* (Se 3*d*) core level shifts +0.42 eV (−0.34 eV) relative to that detected after the 200 °C FG anneal, which is consistent with a decreased concentration of Sc within the $W_xSc_ySe_z$ compound and a corresponding increased oxidation state of the associated W^{x+} component (figure S8). Thermodynamics indicates an additional anneal performed either for a longer period or at a higher temperature could completely dissociate Sc from $W_xSc_ySe_z$, potentially impacting contact resistance further. The gas line connecting the pressurized FG cylinder with the UHV annealing chamber was opened to the chamber overnight to remove adsorbed contaminants from the gas line before performing the FG anneals. However, the specific (presumably negligible) concentration of oxygen-based impurities within the FG and the associated effects on the scandium oxide concentration in the Sc film is not known in detail. Employing a molecular sieve in the gas line between the FG and the annealing chamber could cause additional variations in the chemistry and performance of the Sc contact to WSe_2.

The 200 °C FG anneal converts nearly all of the deposited Sc into either $W_xSc_ySe_z$ or Sc_xO_y (figure 3(b)). The intensity of the chemical state in the Sc 2*p* core level corresponding with the Sc–Se bond decreases by 64.1% during the 200 °C FG anneal. The Sc–Se contribution to the total intensity of the Sc 2*p* core level spectrum decreases to 18% and 5% after the 300 °C and 400 °C FG anneals, respectively (figures 3(b) and (c)), which contrasts the relatively stable intermetallic concentration throughout the UHV anneals. The ScN and ScC chemical states detected after the 200 °C FG anneal fall below the limit of XPS detection after the 400 °C FG anneal. This suggests the partial pressure of H_2 in the FG ambient dissociates Sc–C and Sc–N bonds, which is an energetically favorable process (the energy liberated when a H–H bond is broken is greater than the BDE_{ScC} and BDE_{ScN}) [46].

This work indicates a Sc contact to WSe_2 will completely oxidize when the post-metallization anneal is performed in FG, provided the anneal is performed at a high enough temperature or for a long enough time. Complete Sc–Se, Sc–C, and Sc–N bond dissociation in the presence of oxygen-containing species (i.e. the background gases in a vacuum chamber) are energetically favorable considering either the thermodynamics (see earlier sections for relevant ΔG_f°)orthekinetics($BDE_{Sc–O} > BDE_{Sc–N} > BDE_{Sc–C} > BDE_{Sc–Se} > BDE_{Sc–Sc}$) [46] of the system. The effects of the increased Sc_xO_y concentration on the band alignment and performance of the Sc contact to WSe_2 will be discussed in detail later.

Multiple WSe_2 layers consumed by thermally exacerbated reactions with Sc

The experiments discussed above were performed on bulk WSe_2, which provides an appropriate platform to characterize effects of certain post metallization anneals on the metal-TMD interface chemistry and band alignment. However, FETs are typically fabricated with single and few layer TMDs. In addition, edge contacts exhibit superior performance compared to top contact analogs according to DFT calculations [48, 49] and experimental demonstrations [21, 49]. The true structure of the contact (edge versus top) will be affected by reactions at the metal-TMD interface. In addition, the broken inversion symmetry in WSe_2 films with D_{3h} symmetry is critical to the unique giant spin–orbit splitting in the valence band in the absence

of an out-of-plane electric field [29]. It is therefore of interest to quantify the number of WSe_2 layers affected by reactions with Sc.

Variations in structural and electronic properties of single and few layer TMDs due to interactions with a deposited metal have been investigated previously [50–52]. For example, depositing an incomplete coverage metal film on MoS_2 resulted in a complex vibrational response due to metal-induced spatially varying strain across the TMD [51]. In this work, Raman spectroscopy is employed to quantify the number of layers consumed by reactions with Sc via a characteristic, layer number-dependent vibrational mode exhibited by WSe_2. Special care was taken to ensure a full coverage Sc film was deposited (figure S2). In addition, a 10 nm thick Si capping layer was deposited *in situ* after the Sc deposition and the subsequent anneal (where applicable) to prevent any spurious, air-exposure induced changes in the Raman spectra obtained *ex situ* (procedure described in detail elsewhere) [5]. Therefore, any structural changes manifesting in the Raman spectra are attributed to Sc–WSe_2 reactions. It is important to note here the Raman measurements were obtained within 24 h of Sc/Si deposition and the subsequent anneal.

The first (1st) order in-plane (E^1_{2g}) and out-of-plane (A_{1g}) vibrational modes of WSe_2 are degenerate and do not exhibit any discernible characteristic shifts or changes in intensity with layer number [53]. We recently demonstrated the layer number dependent Raman shifts exhibited by the second (2nd) order longitudinal acoustic mode at the M point in the Brillouin zone [2LA(M)] from single layer to five layer WSe_2 [2.5 cm^{-1}, 0.5 cm^{-1}, 0.5 cm^{-1}, and 0.3 cm^{-1} red shifts increasing from one layer (1L, 261.3 cm^{-1}) to 2L, 2L to 3L, 3L to 4L, and 4L to 5L WSe_2] [5]. Therefore, the number of WSe_2 layers remaining after the Sc deposition and subsequent anneal can be accurately determined by tracking the Raman shift of the 2LA(M) mode. A $\lambda = 532$ nm laser is employed here to access the 2LA(M) mode via resonant excitation conditions [54]. The laser power density (0.49 mA μm^{-2}), number of sweeps (5), and exposure time per sweep (5 s) employed in this work were carefully selected according to control experiments performed previously [5] to prevent laser-induced WSe_2 damage. Therefore, spectral changes were confidently interpreted as indicators of chemical interactions between Sc and WSe_2 rather than laser-induced intermixing.

Figures 4(a)–(c) display the Raman spectra obtained from exfoliated 1L, 2L, and 3L WSe_2 flakes before and after depositing 5 nm Sc at RT and subsequent 300 °C UHV or FG anneals. Depositing 5 nm Sc at RT completely quenches the 1st and 2nd order modes of the 1L WSe_2 flake, which indicates 1L WSe_2 is consumed by reactions with Sc at RT (figure 4(a)). The 1.0 and 1.1 cm^{-1} red shifts and slight symmetric broadening exhibited by the 2LA(M) mode detected from the 2L and 3L WSe_2 flakes, respectively, after depositing 5 nm Sc at RT suggest the interfacing reaction products cause stiffening (softening) of the A_{1g} (E^1_{2g}) mode of the underlying WSe_2 [51, 55].

After the 300 °C UHV anneal, the 1st and 2nd order vibrational modes of the 1L and 2L WSe_2 flakes are completely quenched, while the 1st order modes exhibited by the 3L flake are near the limit of detection (figure 4(b)). This suggests at least two and possibly three WSe_2 layers are consumed by reactions catalyzed during the 300 °C UHV anneal. To more explicitly quantify the number of layers consumed during the anneal, the vibrational modes of a 5L WSe_2 flake were also probed throughout the experiment (figure 4(b)). After the anneal, the corresponding 2LA(M) mode exhibits a 1.2 cm^{-1} blue shift, which is consistent with a transition from 5L to 2L WSe_2 [5]. The spectrum obtained from exfoliated 2L WSe_2 (dotted line) is normalized to the 5L WSe_2 spectra to clearly show the similarity between the spectrum of pristine 2L WSe_2 and 5L WSe_2 after Sc deposition and subsequent 300 °C UHV anneal. Therefore, we confidently conclude that three WSe_2 layers are consumed by reactions with Sc during the 300 °C UHV anneal.

Interestingly, 1L WSe_2 exhibits 1st and 2nd order modes above the limit of detection after the 300 °C FG anneal despite significant reactions detected by XPS in this work. In addition, asymmetric broadening towards lower wavenumber is detected in the 1st order modes of all WSe_2 flakes after the FG anneal. This behavior indicates Se^{x+} (liberated by Sc–Se bond scission) reacts with metallic W to form defective WSe_x clusters, which is consistent with the Raman spectrum obtained from a WSe_2 film lacking long range order [55] and also the XPS results displayed in figure 3.

Roughly nine months after characterizing the three different 10 nm Si/5 nm Sc/3L WSe_2/270 nm SiO_2/Si samples with Raman spectroscopy (figures 4(a)–(c)), lamella were milled and imaged by STEM. The corresponding STEM images are shown in figures 4(d)–(f). After Sc deposition at RT (figure 4(d)), nanocrystalline grains with lattice spacing of 0.21 nm are observed in the Sc film, which is consistent with the Sc{111} family of planes [56]. A significant concentration of oxygen is detected by EDS throughout the Sc film (figure S9). However, the lattice spacing of the grains observed in figure 4(d) is not consistent with that of Sc_2O_3 (0.31 nm) [57], which indicates the oxygen is dispersed in amorphous regions of the film between grains. Se and W diffusion into the Sc film is observed in the corresponding EDS (figure 4(d)). The three ~0.7 nm thick stripes of dark contrast coincide with high-Z W atoms and therefore indicate the presence of three WSe_2 layers (figure 4(d)). The top most WSe_2 layer in figure 4(d) appears to have retained its planar structure in some regions, but the contrast is slightly different from the underlying two layers indicating some disruption of the top layer due to intermixing in general agreement with the corresponding Raman spectra in figure 4(a).

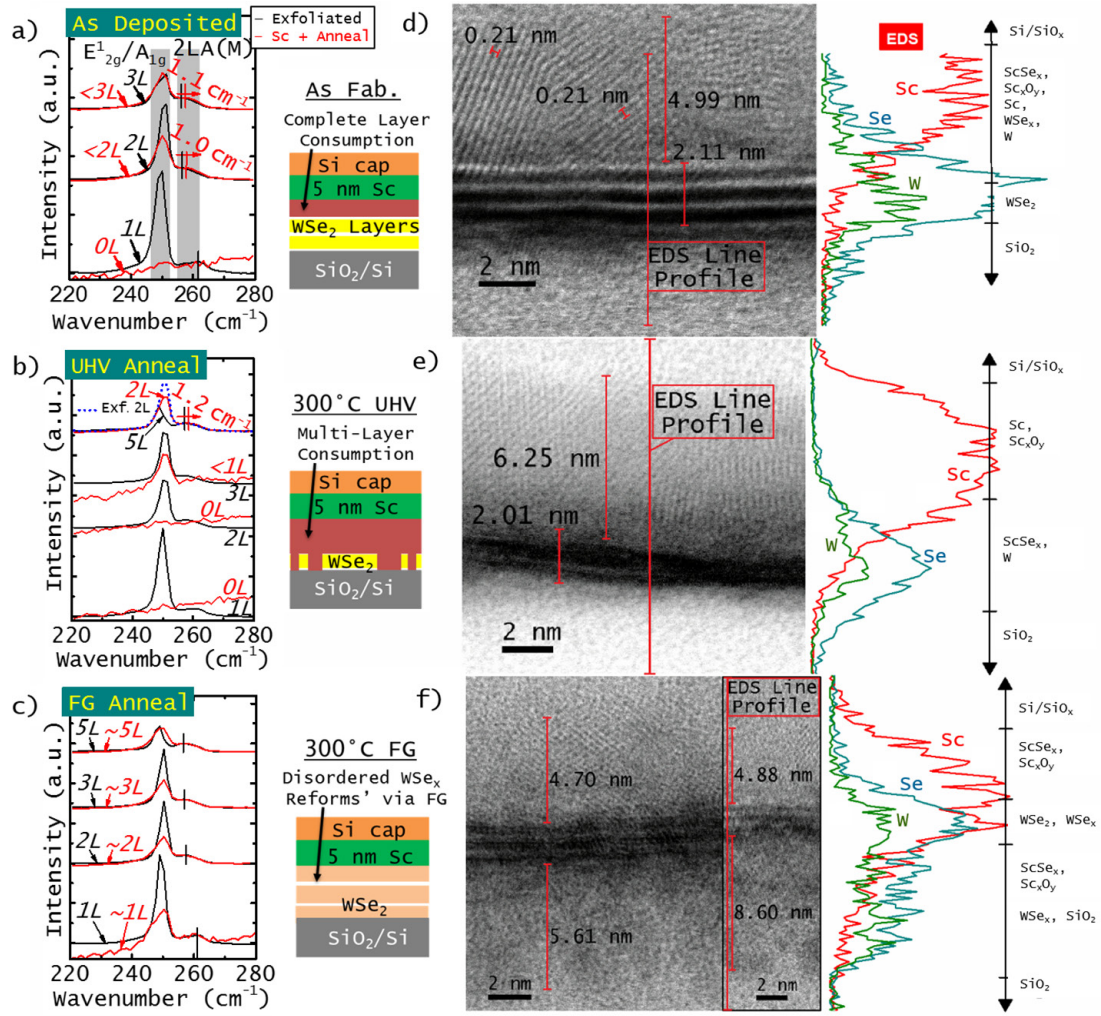


Figure 4. Raman spectra displaying peaks corresponding with the E^1_{2g}, A_{1g}, and 2LA(M) vibrational modes of WSe_2 obtained from 1L, 2L, 3L, and 5L (where applicable) flakes prior to and following (a) 5 nm Sc deposition under UHV conditions and subsequent post metallization anneal at 300 °C in (b) UHV or (c) forming gas. All spectra are normalized to the 2LA(M) peak unless vibrational modes are below the limit of detection. (d)–(f) Cross section STEM images and associated EDS spectra obtained from the same 3L WSe_2 flakes investigated by Raman spectroscopy.

When a lamella is milled from an analogous Sc–WSe_2 sample fabricated at RT in UHV (see supporting information for details) within two weeks of fabrication and imaged immediately, a 2.0–2.5 nm thick amorphous region is observed between Sc and WSe_2 in the corresponding TEM images (figure S10). Therefore, the WSe_2 involved in reactions with Sc undergoes restructuring over time as Sc oxidizes, leading to the physical differences observed by TEM in this work depending on the time between fabrication and imaging.

The thickness of the dark contrast region observed after the 300 °C UHV anneal (~2.0 nm, figure 4(e)) is consistent with that expected of pristine 3L WSe_2. However, individual layers are no longer distinguishable, which suggests significant intermixing occurs between WSe_2 and Sc and corroborates three WSe_2 layers are consumed by reactions during the 300 °C UHV anneal. An amorphous region is observed between the disordered WSe_2 and the polycrystalline Sc film, which likely corresponds with the $ScSe_x$ intermetallic detected by XPS after the same anneal. EDS indicates Se and W diffuse ~3 nm up into the Sc film and down into the SiO_2 substrate. The 0.30 nm lattice spacing exhibited by the nanocrystallites in the Sc film after the anneal (figure 4(e)) indicates the dramatic increase in scandium oxide detected by XPS after the same anneal (figure 2) corresponds with the formation of a polycrystalline Sc_2O_3 film.

After the 300 °C FG anneal, local atomic structure and interlayer van der Waals gaps are resolvable in the corresponding STEM image (figure 4(f)). EDS indicates Se and W diffuse 2–3 nm into the Sc film, while Sc, Se, and W diffuse up to 5 nm into the underlying SiO_2 (dark regions below the WSe_2). Metal diffusion into the underlying dielectric in back-gated devices could impact the device performance (e.g. decreased gate modulation, increased off current). The WSe_2 film is comprised of disordered regions with limited atomic order adjacent regions of 3L WSe_2 with clearly resolvable van der Waals gaps between each layer. These observations corroborate our hypothesis,

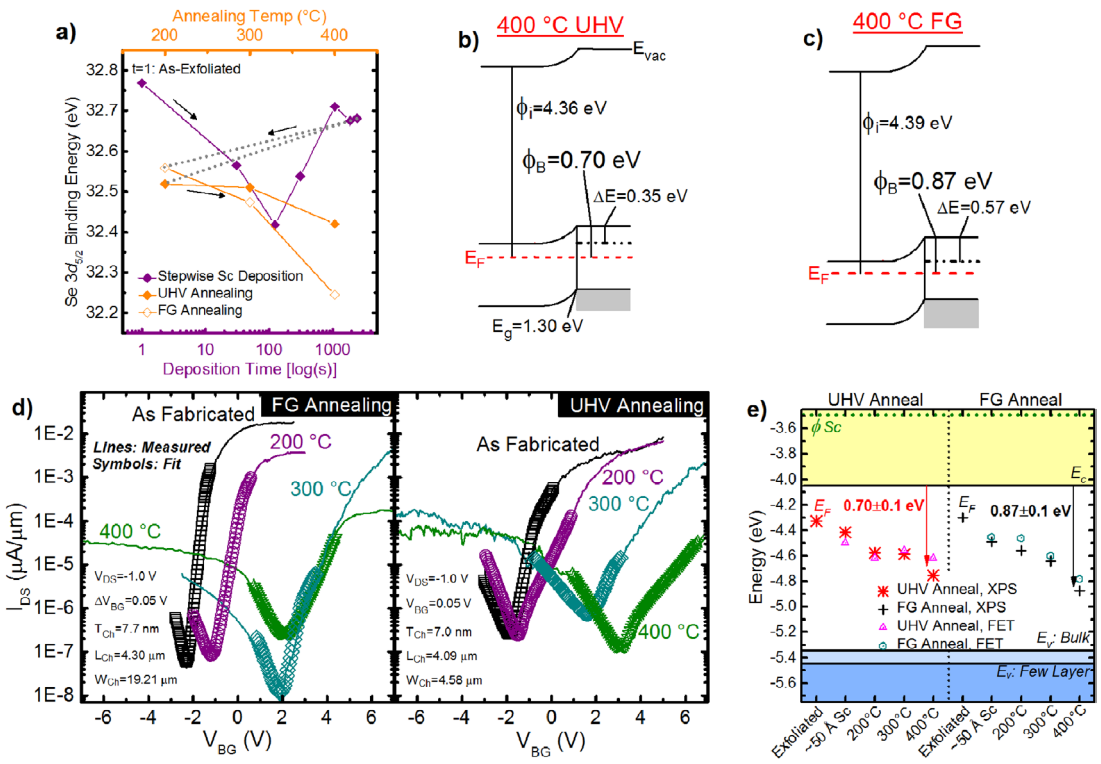


Figure 5. (a) Binding energies of the bulk WSe_2 chemical state in the Se 3*d* core level spectra throughout stepwise Sc deposition and post-metallization annealing in either UHV ♦ or FG ◊ conditions. The BE shifts throughout RT Sc deposition are similar for both samples, which is why the data points obtained from the 'FG anneal' sample prior to the anneals are displayed in (a). Band alignments after the samples are annealed in (b) UHV and (c) FG at 400 °C, which are derived from XPS measurements. The error of ± 0.1 eV is associated with all Fermi level positions depicted. (d) I_{DS}–V_{BG} characteristics (solid lines) measured from back gated few layer WSe_2 FETs with Sc contacts after fabrication and subsequent annealing in UHV or FG. The symbols in (d) correspond with fits of the I_{DS}–V_{BG} obtained with an analytical Schottky barrier model to extract the electron and hole Schottky barrier heights (SBH) throughout the anneals. (e) Band alignment between Sc and WSe_2 after contact deposition and post-metallization anneals according to XPS in (a) and the analytical fits of the I_{DS}–V_{BG} curves in (d). Band diagrams in (b) and (c) are reflected in (e). The ambipolar FET characteristics obtained after FG and UHV anneals corroborate the mid-gap band alignment indicated by XPS.

based on the corresponding XPS (figure 3) and Raman results; W–Se bonds re-form via Sc–Se bond dissociation throughout the FG anneals.

In a device where the contact metal consumes at least one TMD layer, the resulting intermetallic likely remains in intimate lateral contact with the adjacent channel. Therefore, any TMD layers in the contact region consumed by reactions at the metal-TMD interface should be considered pseudo-edge contacts, which may exhibit superior performance to the top contact analog. In addition, understanding changes in the band structure of few layer TMDs associated with interface reaction-induced layer number thinning is critical to engineering superior performance in a wide variety of TMD devices. For instance, maintaining an odd number of layers in the channel of a WSe_2 spin valve is critical to device operation.

Band alignment and electrical performance of the Sc contact to WSe_2

The E_F shifts towards the conduction (valence) band edge will be referred to in the following discussion as positive (negative). Figure 5(a) displays the absolute BEs of the WSe_2 chemical state in the Se $3d_{5/2}$ core level spectra detected from WSe_2 after exfoliation and subsequent stepwise Sc deposition and post-metallization annealing[6].

After exfoliation, the E_F is detected 0.95 ± 0.15 eV from the WSe_2 valence band edge according to the initial valence band offset and secondary electron cutoff (0.95 ± 0.07 eV, 4.36 ± 0.08 eV, respectively; figure S11). The bulk WSe_2 chemical states initially shift to lower BE during the first two Sc depositions. In contrast, the E_F shifts towards higher BE beyond an effective Sc film thickness of 5 Å. The WSe_x and $ScSe_x$ formed during initial Sc depositions likely shift the E_F towards the valence band, while the metallic Sc that accumulates in latter depositions shift the E_F towards the conduction band. Depositing 5.7 nm Sc at RT in UHV shifts the WSe_2 chemical states −0.09 eV (figure 5(a)) from the BEs detected after exfoliation, which corresponds with the formation of a 0.44 ± 0.15 eV electron Schottky barrier. The appreciable Schottky barrier detected here is far from the expected Ohmic electron band alignment expected between Sc and

[6] The separation between the WSe_2 chemical states in the Se $3d_{5/2}$ and W $4f_{7/2}$ core level spectra were held constant throughout Sc deposition and post metallization annealing. Therefore, the binding energies of the WSe_2 chemical state in the W $4f_{7/2}$ core level spectra are omitted from figure 5(a).

WSe_2 considering the low metal work function (3.5 eV) [58]. It is possible the metallic W, formed as a product of the Sc–WSe_2 reaction, dominates the band alignment in an unannealed Sc contact to WSe_2 (polycrystalline tungsten work function ≈4.5 eV) [58].

As the UHV anneal temperature increases, the E_F shift towards lower BE increases in magnitude, exhibiting a total −0.26 eV shift after the 400 °C UHV anneal. The E_F shift corresponds with an increased electron SBH to 0.70 ± 0.15 eV (figure 5(b)).

The band alignment between Sc and a separate bulk WSe_2 crystal after exfoliation, Sc deposition, and subsequent FG anneals (figures 5(a) and (c)) is similar with that detected in the 'UHV anneal' sample. A more detailed discussion of the band alignment between Sc and bulk WSe_2 throughout annealing in FG is provided in the supporting information.

E_F pinning occurs due to gap states in the semiconductor that can be generated by defects, interface reactions, or a deliberately placed re-pinning layer [59]. An appreciable concentration of oxygen deficient Sc_xO_y in the Sc film could generate gap states in the underlying WSe_2, producing the near-midgap alignment detected after the 400 °C anneals. When annealing is performed in UHV, the chemistry, and therefore the electrostatics of the junction, are also convoluted by $ScSe_x$. The Ohmic hole band alignment reported recently between Pd and WSe_2 after a 400 °C FG anneal was facilitated by passivating defects at the interface with atomic hydrogen in the FG ambient [5]. However, the beneficial effects of hydrogen-induced defect passivation on the Sc contact to WSe_2 are either negligible compared with the interface chemistry effects or require hydrogen radicals, which are not readily catalyzed from H_2 by Sc as they are in Pd.

To corroborate the XPS-derived near-midgap band alignment with the electrical performance of Sc contacts to WSe_2, back-gated, few-layer WSe_2 FETs were fabricated on an Al_2O_3/Si substrate with 20 nm Sc/50 nm Pd/100 nm Au contacts. It is difficult to accurately extract SBHs from ultra-thin body transistors in which the depletion width is defined by the thickness of the region under the contacts, such as in few-layer TMD FETs. Therefore, an analytical Schottky barrier model based on Landauer transport theory [14] was employed here to extract electron and hole SBHs from the measured I_{DS}–V_{BG} characteristics of our few layer WSe_2 FETs with Sc contacts. The model, which has been employed in recent works [14, 15, 26, 27], accounts for thermionic emission and the appreciable tunneling contribution to the total current due to the ultra-thin body of the devices. After fabrication, the Sc–WSe_2 FETs exhibit impressive I_{ON}/I_{OFF} ratios in the order of 10^6, subthreshold slope (SS) of 109 mV dec^{-1} (among the best reported to date) [16], and electron SBHs of 0.4–0.45 eV (figure 5(d)), which are in good agreement with the corresponding XPS-derived 0.36–0.44 eV electron SBH (figure 5(e)). Analogous WSe_2 FETs with Pd contacts exhibit a larger 0.73 eV electron SBH, which is likely attributed to photoresist residue-induced E_F pinning [5, 24]. Sc mitigates E_F pinning effects induced by photoresist residue in as-fabricated devices by reacting with the WSe_2 at RT and 'cleaning' resist residue from the interface. Reactions between Sc and common resist polymers are favorable considering Sc–C, Sc–N, and Sc–O bonds are all detected in a resist-free Sc–WSe_2 system, as discussed earlier.

The 400 °C UHV and FG anneals convert 59.9% and 94.9% of the Sc film to Sc_xO_y, respectively. According to the analytical Schottky barrier model, the UHV and FG anneals increase the electron SBH to 0.70 eV and 0.87 eV, respectively (figures 5(d) and (e)). The additional 0.17 eV E_F shift towards the valence band detected after the FG anneals could be related to the much higher Sc_xO_y concentration within the deposited film, considering the charge neutrality level of Sc_2O_3 (~5.3 eV) [28, 40] aligns closely with the WSe_2 valence band edge. In addition, the I_{ON}/I_{OFF} ratio decreases by ~10^3 and the SS increases by approximately a factor of 10 after the UHV and FG anneals. High performance Sc electron contacts to BP have recently been demonstrated [26, 27]. One study correlates significant improvements in n-type device performance with the formation of a Sc_xO_y layer between the Sc contact and BP over one month in ambient conditions [27]. Sc_xO_y formed in the presence of hydroxide molecules (e.g. gettered from air), such as the Sc_xO_y that formed over time at the Sc–BP interface, contains a significant concentration of hydrogen (figure S7), which presumably affects the conductivity. The anneals performed in this work dehydrogenate the Sc_xO_y in the Sc films on WSe_2 [28] resulting in the degraded performance measured with increasing anneal temperature. Therefore, post-metallization anneals in a reducing environment (e.g. UHV or FG) should be avoided to prevent device performance degradation, maximize the gate modulation, minimize the turn-on voltage, and maintain a low electron SBH when Sc contacts are employed.

Controlling the contact polarity by inserting a Sc_xO_y interlayer

E_F depinning at the contacts in devices based on 2D materials has been achieved by inserting a tunnel barrier [15, 60] or 're-pinning' layer [59] between the contact and the channel. Sc_xO_y has only recently been explored, albeit unintentionally, as an interlayer to control contact performance [27]. In this work, WSe_2 was treated with atomic hydrogen to etch the surface, which promotes surface oxidation *in situ* in UHV (figure S12, see supporting information for details). Pd/Sc contacts were then deposited *in situ,* in UHV, at RT, and through a shadow mask to reactively form a Sc_xO_y interlayer between the metal and the WSe_2. Sc scavenges oxygen from WO_x during the UHV deposition, forming an interfacial Sc_xO_y layer. A 3 nm Sc film was deposited on one sample to form

an interlayer entirely comprised of intermetallics and Sc_xO_y and therefore facilitate hole dominant conduction via the Pd layer. 15 nm Sc was deposited on another atomic hydrogen-treated sample to form a substantial metallic Sc layer between the Sc_xO_y interlayer and the Pd capping layer, which facilitates electron dominant conduction.

The forward bias currents measured from the 65 nm Pd/5 nm Sc/WSe_2 diodes were transformed according to equation (1) [62]

$$\frac{I}{1-e^{\frac{qV}{kT}}} \quad (1)$$

where I, q, V, k, and T represent the measured current, electron charge, applied bias, Boltzmann's constant, and temperature, and the linear region in each curve between 0.15 V and 0.35 V was fitted using linear regression. The Richardson constant (33.9 A cm^{-2} K^{-2}, $m_e^* = 0.33$) [63], SBH (0.85 eV), and an ideality factor (1.00, averaged from 5 diodes) are calculated from the slope and intercept of the best fit line to the I–V curve obtained at 110 °C (figures S13(a) and (b), see supporting information for details) [62]. An ideality factor of 1.00 indicates the barrier height is homogeneous across the interface. This suggests the atomic hydrogen treatment coupled with the Sc_xO_y interlayer eliminate defects at the interface unlike the highly inhomogeneous barrier formed at the inert Pd–WSe_2 interface at RT. However, the E_F resides much closer to midgap when the Sc_xO_y interlayer is included between Pd and WSe_2 compared with the Ohmic hole band alignment exhibited by Pd contacts to WSe_2 at RT [5]. Some metallic Sc is likely present within the interlayer and contributes to the near-midgap alignment measured here.

The transformed, annealing-temperature-dependent I–V curves obtained from the 65 nm Pd/15 nm Sc/WSe_2 Schottky diodes yield ideality factors >3 in all cases, which indicates the corresponding SBH will be unreliable. However, an Arrhenius plot of the reverse bias I–V characteristics of the 65 nm Pd/15 nm Sc/WSe_2 Schottky diodes yields a linear pattern, from which a 0.34 eV electron SBH is extracted. The 0.34 eV electron SBH obtained with the 15 nm Sc layer deposited onto the atomic hydrogen-treated WSe_2 is 0.51 eV smaller than the diodes where only 3 nm Sc was deposited (figures 6 and S13(c)) and ~0.1 eV less than Sc–WSe_2 FETs after metallization at RT. The contact structures, fabrication and processing details, and SBHs of all devices from this work are summarized in table 1. Therefore, electron dominant conduction is facilitated by the low work function metallic Sc layer that accumulates on top of the interfacial Sc_xO_y. More effective E_F depinning may be achievable with scandium oxide by tuning the Sc_xO_y layer to minimize the thickness and maximize the tunneling current or by directly depositing the Sc_xO_y rather than depositing metallic Sc on oxidized WSe_2.

The electron Schottky barrier formed between Sc and WSe_2 can be reduced by limiting the intermetallic concentration (i.e. minimizing intermetallic-induced gap states). The contact structure, fabrication and processing details, and employing an optimized, oxygen deficient Sc_xO_y interlayer will minimize reactions with WSe_2 and also provide greater E_F control when other contact metals are employed in conjuction with the interlayer.

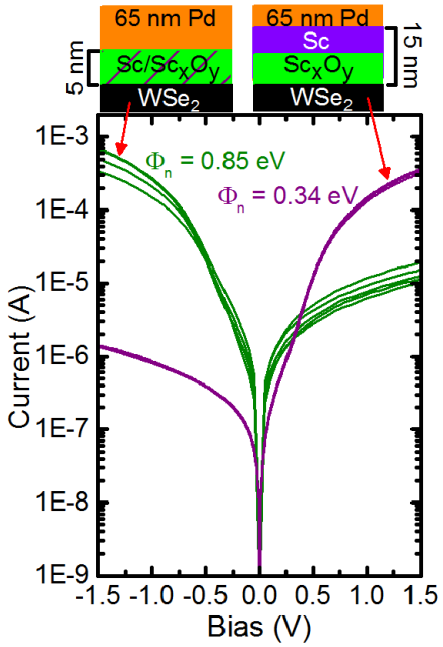


Figure 6. I–V characteristics obtained from Pd–Sc–WSe_2 Schottky diodes deliberately treated with atomic hydrogen before metallization to form an interfacial Sc_xO_y interlayer.

Local density of states around Sc atoms/clusters on WSe_2: STM and STS

The Sc–WSe_2 diodes and FETs discussed above exhibit appreciable 0.4–0.45 eV electron SBHs at RT, which is unexpected considering the work function of Sc (~3.5 eV) is smaller than the electron affinity of WSe_2 (~4.1 eV) [9, 61]. Scanning tunneling microscopy (STM) and spectroscopy (STS) elucidate the surface topography and local density of states (LDOS). Therefore, STM and STS can provide insight into changes in the electronic structure of the WSe_2 surface induced by Sc in the earliest stages of metallization (i.e. after depositing a <3 Å Sc film). The exfoliated WSe_2 surface before metallization is atomically flat with a random distribution of atomic scale defects across the surface, similar to previously published STM images from bulk WSe_2 [9]. The upper and lower STM images in figure 7(a) were obtained *in situ* under positive and negative tip bias, respectively, from exfoliated, bulk WSe_2 after depositing ~1 Å Sc in UHV at RT. Sc atoms/clusters appear as small bright spots surrounded by large dark regions under forward bias, while they appear as large bright patches and ~2 nm diameter rings under reverse bias. The dark contrast exhibited by Sc regions in positive bias indicate an associated

Table 1. Schottky diode and FET contact structure, fabrication details, and electron SBH after processing.

Sc Thickness	Pd Thickess	Anneal Temperature	Anneal Ambient	Atomic Hydrogen Treatment	Electron SBH
20 nm	50 nm	N/A	N/A	N/A	0.44 eV
20 nm	50 nm	400 °C	UHV	N/A	0.70 eV
20 nm	50 nm	400 °C	95% N_2, 5% H_2	N/A	0.87 eV
3 nm	65 nm	N/A	N/A	45 min	0.85 eV
15 nm	65 nm	N/A	N/A	45 min	0.34 eV

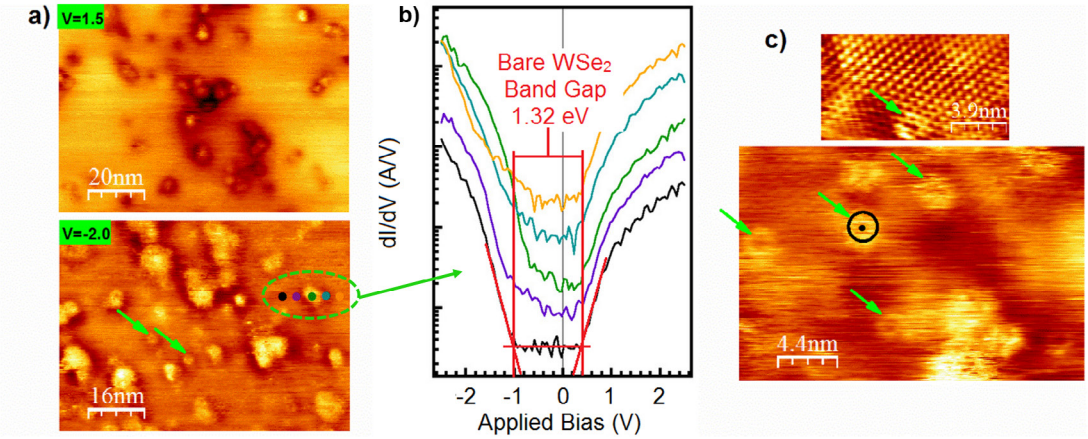


Figure 7. (a) STM images obtained from WSe_2 after a ~1 Å Sc film was deposited in UHV with the upper (lower) image obtained at 1.5 V and 0.5 A (−1.8 V and 0.8 A). (b) STS conductance spectra obtained from points spanning a ~3 nm diameter Sc cluster and the surrounding WSe_2 showing the significant increase in density of states below the WSe_2 E_F when the tip probes directly over the Sc cluster. Each spectrum is a differentiated average of 20 sweeps over the same spot. The spectra are manually offset to more clearly show the features in each spectrum. (c) High resolution STM images obtained from the same 1 Å Sc–WSe_2 sample showing atomic resolution in a region of bare WSe_2, rings of bright contrast reflecting charge redistribution around single Sc atoms (some indicated by green arrows), and larger Sc clusters.

high resistance tunneling barrier and therefore fewer occupied LDOS. Sc oxidation occurs in UHV and therefore could contribute to the suppressed LDOS around Sc when 'filled' states are probed.

Five STS spectra were obtained in an array spanning a Sc cluster and the surrounding WSe_2 (dots in figure 7(a), lower image). The bare WSe_2 exhibits a band gap of 1.32 ± 0.05 eV, which is consistent with previous STM studies of bulk WSe_2 (figure 7(b)) [9]. The E_F is detected 0.33 ± 0.05 eV from the valence band edge, which is consistent with the XPS-derived band alignment of exfoliated WSe_2 in this work. As the tip approaches the Sc cluster, the reverse bias conductance and density of gap states below the E_F increase and reach a maximum when the tip is positioned directly over it. The enhanced density of states in the valence band observed over Sc clusters is qualitatively consistent with the E_F shift away from the conduction band detected by XPS after depositing Sc on WSe_2.

In high resolution reverse bias images (figure 7(c)), individual Sc atoms and the associated Sc–Se bonds are inferred from numerous ~2 nm diameter rings of bright contrast (pointed out by arrows). These regions exhibit central symmetry, which suggests a 1D feature (i.e. a single atom) is present at the center. Similar features were observed via STM around isolated Mo atoms at interstitial sites in the $MoTe_2$ lattice [61]. The ring of bright contrast observed in reverse bias images manifests as a result of charge transfer from Sc to the surrounding Se atoms, similar to the charge redistribution associated with mirror twin boundaries in TMDs. Therefore, the formation of Sc–Se bonds and the associated enhanced density of states below the WSe_2 E_F contribute significantly to the unexpectedly high electron Schottky barrier formed between the Sc contact and WSe_2.

Discussion

The physical characterization, E_F shifts according to XPS, and electrical characteristics of Schottky diodes and FETs indicate the WSe_2 FETs exhibit the lowest electron SBH, the highest I_{ON}/I_{OFF} ratio (~10^6), and the steepest SS (109 mV dec^{-1}) when the intermetallic concentration at the Sc–WSe_2 interface is minimized and the concentration of metallic Sc within the contact is maximized. In this work, the lowest electron SBH between Sc and WSe_2 (0.34 eV) is achieved by oxidizing the WSe_2 surface prior to Sc deposition, which both limits the Sc–WSe_2 reaction and avoids the deleterious post-metallization anneals. Inserting an inert, oxygen-free tunneling layer (e.g. hBN) [15] between Sc and WSe_2 would more effectively prevent the Sc–WSe_2 reactions and decrease oxygen concentration in the

Sc layer compared to the reactively formed Sc_xO_y interlayer employed in this work, likely resulting in the highest performance Sc contact to WSe_2. Sc immediately consumes one WSe_2 layer at RT and at least three layers during the post-metallization anneals. This work establishes relationships between the Sc–WSe_2 interface chemistry, structure, and band alignment associated with specific pre- and post-metallization processing steps, which are integral to engineering consistent, high-performance Sc contacts to any TMD. Critically, we demonstrate high performance n-type WSe_2 FETs with Sc contacts and establish processing conditions (both to employ and to avoid) for consistent, high-performance n-type Sc contacts.

Conclusions

This work demonstrates high-performance n-type WSe_2 FETs with impressive I_{ON}/I_{OFF} (10^6) and SS (109 mV dec^{-1}), which is achieved without any post-metallization processing and by depositing the Sc contacts in UHV. Mildly oxidizing the WSe_2 surface at the contact regions before metallization reduces the electron SBH formed between Sc and WSe_2 at RT by 0.10 eV as a direct result of the minimized concentration of scandium selenide at the interface. The largest electron SBHs of 0.70 eV and 0.87 eV (400 °C UHV and FG, respectively) worst SS (~1 V dec^{-1}), and lowest I_{ON}/I_{OFF} ratios (~10^3) are measured when post-metallization anneals are employed, which contrasts the highest performance Pd contacts to WSe_2 after the same anneal. XPS indicates the anneals increase the electron SBH by 0.4–0.5 eV and completely oxidize the Sc contact, which cause the aforementioned degraded device performance. STM and STS explicitly relate the unexpectedly large electron SBH observed between Sc and WSe_2 throughout this work with an enhanced LDOS below the WSe_2 E_F in the presence of Sc–Se bonds, which necessitates processing steps that minimize the Sc–WSe_2 reaction. The significant reactions between Sc and WSe_2 are corroborated by Raman spectroscopy and STEM, which indicate 1L WSe_2 is consumed at RT and at least three WSe_2 layers are consumed during the anneals. The processing condition-dependent number of WSe_2 layers consumed by Sc is a critical benchmark for future device architectures based on WSe_2, especially those relying on the giant spin-Hall effect that occurs in WSe_2 with D_{3h} symmetry. This work shows a detailed understanding of the relationships between processing conditions, interface chemistry, and contact performance can be leveraged in any metal–TMD system to consistently achieve the highest device performance.

Acknowledgment

The authors would like to thank A Yu (Massachusetts Institute of Technology) and M J Mleczko (Intel) for useful discussions regarding the analytical Schottky barrier fitting procedure and the Landauer theory behind the model. The support of Prof P Hurley at the Tyndall National Institute/University College Cork Ireland is also gratefully acknowledged. This work was supported in part by NSF Award No. 1407765 under the US/Ireland UNITE collaboration and by the Semiconductor Research Corporation (SRC) as the NEWLIMITS Center and NIST through award number 70NANB17H041. This work has also received funding in part from the European Union's Horizon 2020 research and innovation program under the Marie Skłodowska-Curie grant agreement No 713567 and a research grant from Science Foundation Ireland (SFI) under Grant Number SFI/12/RC/2278.

Supporting information

C 1*s* and O 1*s* core levels obtained from WSe_2 after Sc deposition in UHV and HV; calibrating the Sc 3*s* and Sc 3*p* core level BE and intensity; calculating stoichiometry based on XPS; chemical state evolution throughout stepwise Sc deposition and post metallization annealing in UHV; evidence of Sc–C, Sc–N, and Sc–O bonding; chemical state evolution throughout Sc deposition and post metallization annealing in FG; determining the critical Sc and Si thickness for full coverage films; EDS including the oxygen spectra; TEM image of the Pd–Sc–WSe_2 structure two weeks after fabrication; SBH extraction from Schottky diode *I*–*V* characteristics; constructing band diagrams from XPS measurements; oxidized WSe_2 after atomic hydrogen treatment; valence band edge and secondary electron cutoff from exfoliated WSe_2; AFM images of exfoliated single and few layer WSe_2 flakes.

Conflict of interest

The authors declare no competing financial interest.

ORCID iDs

Lee A Walsh https://orcid.org/0000-0002-6688-8626
Christopher L Hinkle https://orcid.org/0000-0002-5485-6600
Robert M Wallace https://orcid.org/0000-0001-5566-4806

References

[1] Abraham M and Mohney S E 2017 Annealed Ag contacts to MoS_2 field-effect transistors *J. Appl. Phys.* **122** 115306
[2] Wu Y, Xiang J, Yang C, Lu W and Lieber C M 2004 Single-crystal metallic nanowires and metal/semiconductor nanowire heterostructures *Nature* **430** 61–5
[3] Lin J C, Yu S Y and Mohney S E 2016 Characterization of low-resistance ohmic contacts to N- and P-type InGaAs *J. Appl. Phys.* **114** 044504

[4] Walsh L A, Hughes G, Weiland C, Woicik J C, Lee R T P, Loh W Y, Lysaght P and Hobbs C 2014 Ni-(In,Ga)As alloy formation investigated by hard-x-ray photoelectron spectroscopy and x-ray absorption spectroscopy *Phys. Rev. Appl.* **2** 064010

[5] Smyth C M *et al* 2019 Engineering the palladium-WSe_2 interface chemistry for field effect transistors with high performance hole contacts *ACS Appl. Nano Mater.* **2** 75–88

[6] Allain A, Kang J, Banerjee K and Kis A 2015 Electrical contacts to two-dimensional semiconductors *Nat. Mater.* **14** 1195–205

[7] Addou R *et al* 2015 Impurities and electronic property variations of natural MoS_2 crystal surfaces *ACS Nano* **9** 9124–33

[8] McDonnell S, Addou R, Buie C, Wallace R M and Hinkle C L 2014 Defect dominated doping and contact resistance in MoS_2 *ACS Nano* **8** 2880–8

[9] Addou R and Wallace R M 2016 Surface analysis of WSe_2 crystals: spatial and electronic variability *ACS Appl. Mater. Interfaces* **8** 26400–6

[10] Smyth C M, Addou R, McDonnell S, Hinkle C L and Wallace R M 2016 Contact metal-MoS_2 interfacial reactions and potential implications on MoS_2-based device performance *J. Phys. Chem.* C **120** 14719–29

[11] Smyth C M, Addou R, McDonnell S, Hinkle C L and Wallace R M 2017 WSe_2-contact metal interface chemistry and band alignment under high vacuum and ultra high vacuum deposition conditions *2D Mater.* **4** 025084

[12] McDonnell S, Smyth C, Hinkle C L and Wallace R M 2016 MoS_2-titanium contact interface reactions *ACS Appl. Mater. Interfaces* **8** 8289–94

[13] Joo M-K, Moon B H, Ji H, Han G H, Kim H, Lee G, Lim S C, Suh D and Lee Y H 2016 Electron excess doping and effective Schottky barrier reduction on the MoS_2/h-BN heterostructure *ACS Nano* **16** 6383–9

[14] Penumatcha A V, Salazar R B and Appenzeller J 2015 Analysing black phosphorous transistors using an analytic Schottky barrier MOSFET model *Nat. Commun.* **6** 8948

[15] Mleczko M J, Yu A C, Smyth C M, Shin Y C, Chen V, Tsai Y-C, Nishi Y, Wallace R M and Pop E 2019 Contact engineering high performance n-type $MoTe_2$ transistors *Nano Lett.* submitted

[16] Prakash A and Appenzeller J 2017 Bandgap extraction and device analysis of ionic liquid gated WSe_2 Schottky barrier transistors *ACS Nano* **11** 1626–32

[17] Appenzeller J, Zhang F, Das S and Knoch J 2016 Transition metal dichalcogenide Schottky barrier transistors: a device analysis and material comparison *2D Materials for Nanoelectronics* ed M Houssa *et al* (New York: Taylor & Francis) pp 207–40

[18] McDonnell S, Azcatl A, Addou R, Gong C, Battaglia C, Chuang S, Cho K, Javey A and Wallace R M 2014 Hole contacts on transition metal dichalcogenides: interface chemistry and band alignments *ACS Nano* **8** 6265–72

[19] Chuang H J, Chamlagain B, Koehler M, Perera M M, Yan J, Mandrus D, Tománek D and Zhou Z 2016 Low-resistance 2D/2D Ohmic contacts: a universal approach to high-performance WSe_2, MoS_2, and $MoSe_2$ transistors *Nano Lett.* **16** 1896–902

[20] Cho S *et al* 2015 Phase patterning for Ohmic homojunction contact in $MoTe_2$ *Science* **349** 625–8

[21] Kappera R, Voiry D, Yalcin S E, Branch B, Gupta G, Mohite A D and Chhowalla M 2014 Phase-engineered low-resistance contacts for ultrathin MoS_2 transistors *Nat. Mater.* **13** 1128–34

[22] Sung J H *et al* 2017 Coplanar semiconductor–metal circuitry defined on few-layer $MoTe_2$ via polymorphic heteroepitaxy *Nat. Nanotechnol.* **12** 1064–70

[23] Liu W, Kang J, Sarkar D, Khatami Y, Jena D and Banerjee K 2013 Role of metal contacts in designing high-performance monolayer N-type WSe_2 field effect transistors *Nano Lett.* **13** 1983–90

[24] Bolshakov P, Smyth C M, Khosravi A, Zhao P, Hurley P K, Hinkle C L, Wallace R M and Young R M 2019 Contact engineering for dual-gate MoS_2 transistors using O_2 plasma exposure *ACS Appl. Electron. Mater.* **1** 210

[25] Das S, Chen H Y, Penumatcha A V and Appenzeller J 2013 High performance multilayer MoS_2 transistors with scandium contacts *Nano Lett.* **13** 100–5

[26] Wang C-H, Incorvia J A C, McClellan C J, Yu A C, Mleczko M J, Pop E and Philip Wong H-S 2018 Unipolar n-type black phosphorous transistors with low work function contacts *Nano Lett.* **18** 2822–7

[27] Li L, Engel M, Farmer D B, Han S-J and Philip Wong H-S 2016 High-performance p-type black phosphorous transistor with scandium contact *ACS Nano* **10** 4672–7

[28] Liu A, Liu G, Zhu H, Song H, Shin B, Fortunato E, Martins R and Shan F 2015 Water-induced scandium oxide dielectric for low-operating voltage n- and p-type metal-oxide thin-film transistors *Adv. Funct. Mater.* **25** 7180–8

[29] Zhu Z Y, Cheng Y C and Schwingenschlogl U 2011 Giant spin-orbit-induced spin splitting in two-dimensional transition-metal dichalcogenide semiconductors *Phys. Rev.* B **84** 153402

[30] Shao Q, Yu G, Lan Y-W, Shi Y, Li M-Y, Zheng C, Zhu X, Li L-J, Amiri P K and Wang K L 2016 Strong Rashba–Edelstein effect-induced spin-orbit torques in monolayer transition metal dichalcogenide/ferromagnet bilayers *Nano Lett.* **16** 7514–20

[31] HQ Graphene www.hqgraphene.com (Accessed: 11 July 2019)

[32] Wallace R M 2008 *In situ* studies of interfacial bonding of high-k dielectrics for CMOS beyond 22 nm *ECS Trans.* **16** 255–71

[33] Wallace R M 2014 *In situ* studies on 2D materials *ECS Trans.* **64** 109–16

[34] ASTM E2108-16 *Standard Practice for Calibration of the Electron Binding-Energy Scale of an X-Ray Photoelectron Spectrometer, in ASTM Volume 03.06 Molecular Spectroscopy and Separation Science; Surface Analysis, ASTM International, West Conshohocken, Pennsylvania, USA.*

[35] Herrera-Gómez A, Hegedus A and Meissner P L 2002 Chemical depth profile of ultrathin nitrided SiO_2 films *Appl. Phys. Lett.* **81** 1014–6

[36] Bolshakov P, Zhao P, Azcatl A, Hurley P K, Wallace R M and Young C D 2017 Improvement in top-gate MoS_2 transistor performance due to high quality backside Al_2O_3 layer *Appl. Phys. Lett.* **111** 032110

[37] University of Texas at Dallas Cleanroom www.utdallas.edu/research/cleanroom/ (Accessed: 11 July 2019)

[38] Freedy K M, Giri A, Foley B M, Barone M R, Hopkins P E and McDonnell S 2018 Titanium contacts to graphene: process-induced variability in electronic and thermal transport *Nanotechnology* **29** 145201

[39] Pauling L 1960 *The Nature of the Chemical Bond* 3rd edn (New York: Cornell Univ. Press)

[40] Gila B P *et al* 2001 Gadolinium oxide and scandium oxide: gate dielectrics for GaN MOSFETs *Phys. Status Solidi* **188** 239–42

[41] Weast R C, Lide D R, Astle M J and Beyer W H 1995 Selected values of chemical thermodynamic properties *CRC Handbook of Chemistry and Physics* (Boca Raton, FL: CRC Press)

[42] Sidorko V R, Goncharuk L V, Gordiychuk O V and Antonchenko R V 1995 Thermodynamic properties of scandium carbides *J. Alloys Compd.* **228** 159–63

[43] Porte L 2000 Stoichiometric ScN and nitrogen deficient scandium nitride layers studied by photoelectron spectroscopy *J. Phys. C: Solid State Phys.* **18** 6701–9

[44] Zhao P, Azcatl A, Bolshakov P, Moon J, Hinkle C L, Hurley P K, Wallace R M and Young C D 2017 Effects of annealing on top-gated MoS_2 transistors with HfO_2 dielectric *J. Vac. Sci. Technol.* B **35** 01A118

[45] Amani M *et al* 2015 Near-unity photoluminescence quantum yield in MoS_2 *Science* **350** 1065–8

[46] Luo Y-R 2007 *Comprehensive Handbook of Chemical Bond Energies* (Boca Raton, FL: CRC Press)

[47] Sevy A, Huffaker R F and Morse M D 2017 Bond dissociation energies of tungsten molecules: WC, WSi, WS, WSe, and WCl *J. Phys. Chem.* A **121** 9446–57

[48] Kang J, Liu W, Sarkar D, Jena D and Banerjee K 2014 Computational study of metal contacts to monolayer transition-metal dichalcogenide semiconductors *Phys. Rev.* X **4** 031005

[49] Liu W, Kang J, Cao W, Sarkar D, Khatami Y, Jena D and Banerjee K 2013 High-performance few-layer-MoS_2 field-effect-transistor with record low contact-resistance *IEEE Int. Electron Devices Meeting* (https://doi.org/10.1109/IEDM.2013.6724660)
[50] Chen C-H, Wu C-L, Pu J, Chiu M-H, Kumar P, Takenobu T and Li L-J 2014 Hole mobility enhancement and P-doping in monolayer WSe_2 by gold decoration *2D Mater.* **1** 034001
[51] Gong C *et al* 2013 Metal contacts on physical vapor deposited monolayer MoS_2 *ACS Nano* **7** 11350–7
[52] Yuan H *et al* 2015 Influence of metal-MoS_2 interface on MoS_2 transistor performance: comparison of Ag and Ti contacts *ACS Appl. Mater. Interfaces* **7** 1180–7
[53] Zhao W, Ghorannevis Z, Amara K K, Pang J R, Toh M, Zhang X, Kloc C, Tan P H and Eda G 2013 Lattice dynamics in mono- and few-layer sheets of WS_2 and WSe_2 *Nanoscale* **5** 9677
[54] Sahin H, Tongay S, Horzum S, Fan W, Zhou J, Li J, Wu J and Peeters F M 2013 Anomalous Raman spectra and thickness-dependent electronic properties of WSe_2 *Phys. Rev.* B **87** 165409
[55] Shi W, Lin M-L, Tan Q-H, Qiao X-F, Zhang J and Tan P-H 2013 Raman and photoluminescence spectra of two-dimensional nanocrystallites of monolayer WS_2 and WSe_2 *2D Mater.* **3** 25016
[56] Spedding F H, Daane A H and Herrmann K W 1956 The crystal structures and lattice parameters of high-purity scandium, yttrium, and the rare earth metals *Acta Crystallogr.* **9** 559
[57] Feijoo P C, del Prado A, Toledano-Luque M, San Andres E and Lucia M L 2010 Scandium oxide deposited by high-pressure sputtering for memory devices: physical and interfacial properties *Appl. Phys. Lett.* **107** 084505
[58] Michaelson H B 1977 The work function of the elements and its periodicity *J. Appl. Phys.* **48** 4729–33
[59] Chen J-R, Odenthal P M, Swartz A G, Floyd G C, Wen H, Luo K Y and Kawakami R K 2013 Control of Schottky barriers in single layer MoS_2 transistors with ferromagnetic contacts *Nano Lett.* **13** 3106–10
[60] Coss B E, Smith C, Loh W-Y, Majhi P, Wallace R M, Kim J and Jammy R 2011 Contact resistance reduction to FinFET source/drain using novel dipole Schottky barrier height modulation method *IEEE Electron Device Lett.* **32** 862–4
[61] Coelho P M, Komsa H-P, Diaz H C, Ma Y, Krasheninnikov A V and Batzill M 2018 Post-synthesis modifications of two-dimensional $MoSe_2$ or $MoTe_2$ by incorporation of excess metal atoms into the crystal structure *ACS Nano* **12** 3975–84
[62] Schroder D K 2006 *Semiconductor Material and Device Characterization* 3rd edn (Hoboken, NJ: Wiley)
[63] Liu W, Cao W, Kang J and Banerjee K 2013 High-performance field-effect-transistors on monolayer WSe_2 *ECS Trans.* **58** 281–5